Ore Geology Reviews 120 (2020) 103449

Contents lists available at ScienceDirect

Ore Geology Reviews

journal homepage: www.elsevier.com/locate/oregeorev

Three-stage formation of greenstone-hosted orogenic gold deposits in the Val-d'Or mining district, Abitibi, Canada: Evidence from pyrite and tourmaline

Lucille Daver[a,*], Michel Jébrak[a], Georges Beaudoin[b], Robert B. Trumbull[c]

[a] Département des sciences de la Terre et de l'atmosphère, Université du Québec à Montréal, QC, Canada
[b] Département de géologie et de génie géologique, Université Laval, Québec, QC, Canada
[c] German Research Centre for Geosciences GFZ, Telegrafenberg 14473, Potsdam, Germany

ARTICLE INFO

Keywords:
Orogenic gold
Tourmaline
Pyrite
LA-ICP-MS
Element mapping
Boron isotopes
Val-d'Or
Abitibi

ABSTRACT

Orogenic gold deposits are the most widespread type of gold deposit worldwide, defining important exploration targets in Precambrian greenstone belts. Here, we refine the model for orogenic gold formation in the world-class Val-d'Or mining district (Quebec, Canada) using geochemical, isotopic and mineralogical data from quartz-tourmaline-carbonate (QTC) veins from several deposits across the district. Multi-element (Ag, As, Au, B, Ba, Co, Mg, Mo, Ni, and Pb) pyrite mapping, as well as major, trace, and rare earth element variations in tourmaline, define a three-stage paragenesis across several deposits. The first, reduced phase crystallized the quartz-carbonate-gold association in the veins; the second, oxidized phase favored tourmaline and barite crystallization (barite was not previously reported from this district); the third phase involved a reduced fluid and the crystallization of non-auriferous, As-Co-Ni-rich cubic pyrite, and tourmaline. Boron isotope ratios of tourmaline vary from −15.6 to −7.7‰, which is attributed to the mixing of at least two fluids, one related to a deep, metamorphic source and the other to shallower, possibly relict formation water. A systematic regional pattern in B-isotope variation is found, with lighter values in the volcanic rocks and heavier ones in or close to intrusions, which suggests different mixing proportions in the vein field from NE to SW.

1. Introduction

Archean greenstone belts host most of the world's high-grade orogenic gold deposits. Among them, the Abitibi subprovince in the southeastern part of the Precambrian Canadian Shield hosts hundreds of gold deposits, distributed over more than 200 km along two major connected reverse shear zones: the Cadillac-Larder Lake Fault Zone (CLLFZ) to the south and the Porcupine-Destor Fault Zone (PDFZ) to the north (Fig. 1; Robert, 1994). The Val-d'Or mining district is located in the eastern part of the Abitibi subprovince along the CLLFZ. It hosts approximately 55 auriferous quartz-tourmaline-carbonate (QTC) vein deposits spread over a 40 by 15 km area (Fig. 1), which together contain a total of ~20 million ounces Au (Rafini, 2014). In this district, the Sigma QTC auriferous veins have become one of the archetypes of orogenic gold deposits (Sibson et al., 1988; Robert, 1994; Gaboury, 1999; Neumayr and Hagemann, 2002).

Based on structural and hydrothermal characteristics (mineral assemblages and alteration), the Abitibi gold-bearing QTC vein field is commonly understood to represent a single hydrothermal event (Robert, 1994). Mineralization is suggested to have occurred at the end of the formation of the Superior Province (~2.6 Ga), or shortly thereafter, through the process of seismic pumping, whereby fluid transport occurred in seismically-induced pulses (Sibson et al., 1975; Boullier and Robert, 1992). This process resulted in the circulation of mineralized hydrothermal fluids into third-order fault systems of the CLLFZ during earthquake rupturing episodes. However, the precise chronology of this episodic infilling is still debated (Kerrich and Ludden, 2000; Robert et al., 2005).

Previous isotopic studies in the Val-d'Or district (Beaudoin and Pitre, 2005; Beaudoin and Chiaradia, 2016) suggest a fluid mixing scenario for the mineralizing fluid two different fluid reservoirs where the H-O-Sr isotope values of the vein assemblage are interpreted to reflect two end-member fluids: one metamorphic and another supracrustal (Beaudoin and Chiaradia, 2016). A preliminarily tourmaline B-isotope study by Beaudoin et al. (2013) suggested the presence of a regional southwest to northeast isotopic zonation in the district.

* Corresponding author.
E-mail address: daver.lucille@uqam.ca (L. Daver).

https://doi.org/10.1016/j.oregeorev.2020.103449
Received 16 March 2019; Received in revised form 14 February 2020; Accepted 3 March 2020
Available online 09 March 2020
0169-1368/

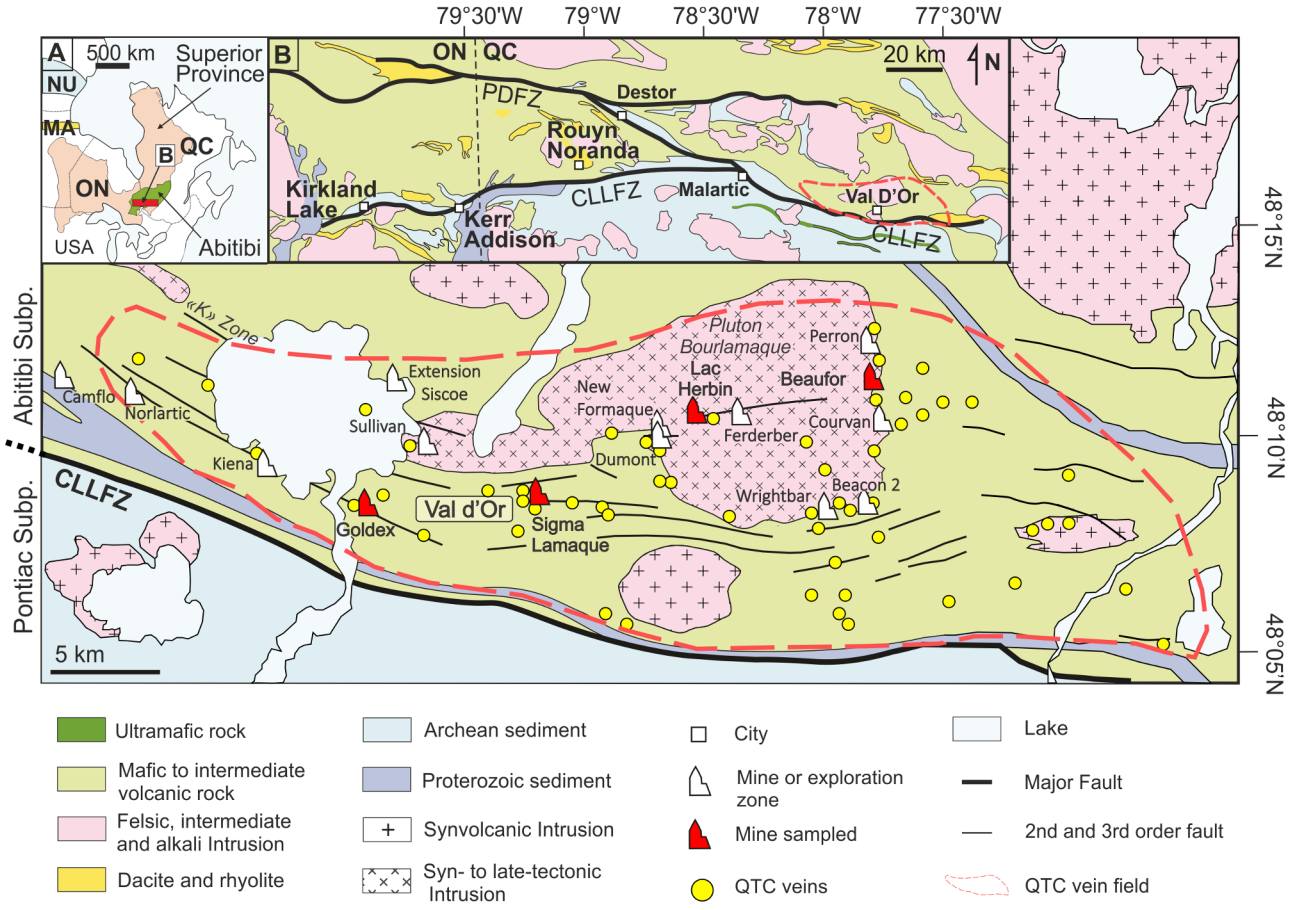

Fig. 1. Simplified map of the Abitibi Greenstone Belt and the Val-d'Or mining district (modified from Neumayr and Hagemann (2002), Robert et al. (2005), and Mériaud and Jébrak (2017)). Red symbols of a mine shaft represent mines sampled as part of this study, which all exploit quartz-tourmaline-carbonate (QTC) auriferous veins, represented by yellow circles. ON = Ontario, QC = Quebec, CLLFZ = Cadillac-Larder Lake fault zone, and PDFZ = Porcupine-Destor fault zone. (For interpretation of the references to colour in this figure legend, the reader is referred to the web version of this article.)

The objective of this study is to improve the understanding of the temporal and genetic relationships of QTC vein mineralogical assemblages in the Val-d'Or district through a detailed investigation of pyrite and tourmaline. The current formation model proposes multiple fluid pulses during a single hydrothermal event involving the mixing of metamorphic and upper crustal fluids (Robert, 1994; Gaboury, 1999; Neumayr and Hagemann, 2002; Beaudoin and Chiaradia, 2016). To better define this model, samples from several deposits distributed across the region were selected to obtain a regional coverage that is representative of the geochemical variability in the vein field (Fig. 1). Pyrite and tourmaline were chosen as the minerals best suited to investigate the paragenetic evolution of the system. Gold in the Val-d'Or district is mainly associated with pyrite, either as inclusions and/or in the pyrite lattice. Pyrite formed episodically during QTC vein formation, and its chemical variability reflects changes in hydrothermal fluid chemistry and in mineralizing conditions (P, T, redox) throughout its mineralization history (Large et al., 2009; Goldfarb and Groves, 2015). Tourmaline has a broad stability range and a wide chemical variability, which responds to changes in fluid composition (Van Hinsberg and Schumacher, 2009; Henry et al., 2011; Dutrow and Henry, 2011). Furthermore, B-isotope variations in tourmaline can effectively fingerprint fluid sources and identify regions where fluid mixing has occurred (Krienitz et al., 2008; Zhang et al., 2014a; Lambert-Smith et al., 2016).

2. Geological setting

2.1. Val-d'Or mining district

The Val-d'Or QTC vein field is located at the tectonic boundary between the Abitibi volcanic subprovince and the Pontiac sedimentary subprovince of the Archean Superior Province (Card and Ciesielski, 1986). The 200 km-long Cadillac-Larder Lake fault is a major shear zone (CLLFZ), which separates these two subprovinces (Fig. 1). It represents a first-order fault, which dips steeply to the north and flattens at approximately 10 km depth (Green et al., 1990; Robert, 1994). Second-order structures consist of 1 to 10 km-long and 1 to 100 m-wide faults with an E-W subvertical strike-slip in the Val-d'Or district (Robert, 1990). The third-order faults are smaller and more numerous, ranging from 1 m to 1 km in length, with strike-slip movement, and trending between NW and NE, dipping 35° to 75° to the south or north (Robert, 1990).

The Val-d'Or mining district is composed of ultramafic to intermediate volcanic rocks emplaced between 2714 Ma and 2702 Ma ± 2 Ma (Pilote et al., 1998; Scott et al., 2002). A series of *syn*-to-late tectonic intrusions dated from 2694 to 2680 Ma, including the Lamaque diorite at 2685 Ma (Jemielita, 1990) and the Bourlamaque pluton at 2699 ± 1 Ma (Hanes et al., 1992; Wong et al., 1991; Jemielita et al., 1990) crosscut the volcanic and intrusive rocks. Regional greenschist facies metamorphism occurred from 2693 to 2677 Ma (Hanes et al., 1992; Feng and Kerrich, 1992) and was accompanied by regional shortening, forming a series of dominant E-W subvertical to moderately-dipping shear zones that host the QTC veins

(Robert, 1990). Regional deformation ended with the convergence of the Abitibi and the Pontiac terranes along the CLLFZ at ~2670 Ma (Feng and Kerrich, 1992).

The district hosts two overlapping auriferous vein types: early quartz-carbonate veins and later quartz-tourmaline-carbonate (QTC) veins. The early quartz-carbonate auriferous vein field formed before regional metamorphism (> 2690 Ma). These veins are folded and boudinaged within sub-vertical shear zones, and crosscut by regional mafic dykes (Robert, 1990). The later, QTC-type veins are the subject of this study. They were emplaced after metamorphism (less than2670 Ma) and are crosscut on a regional scale by Archean intrusions and mafic dykes, but not by Proterozoic dykes (Latulippe, 1966; Robert, 1994; Couture et al., 1994). The QTC veins were emplaced in sub-vertical reverse shear zones as fault-filled lenses, or near the shear zones in sub-horizontal extensional veins (Robert et al., 1995).

These two vein fields are interpreted as having formed in two successive hydrothermal events (Robert, 1994; Robert and Brown, 1986; Couture et al., 1994), which likely shared the same fluid conduit: the first-order fault system (Robert, 1990; Neumayr and Hagemann, 2002; Beaudoin and Pitre, 2005). However, the QTC vein field is better endowed with mineralization, and hosts several economic deposits with similar mineralogical characteristics (Robert and Brown, 1986; Fig. 1). Robert (1994) suggested that the fault system worked as an interconnected system to allow for fluid circulation.

2.2. Sample descriptions

Six QTC veins were sampled from four mines (red symbols in Fig. 1): one from the Goldex mine, three from the Lamaque mine (two from the Triangle and one from the Parallel zones), one from the Lac Herbin mine (production ended in 2016), and one from the Beaufor mine (production ended in 2019). The sampled mines are aligned along with a SW-NE trend across the Val-d'Or mining district (Fig. 1). They occur in two different host lithologies: (1) local diorite intrusions in volcanic rocks (Goldex and Lamaque QTC veins), and (2) the dioritic Bourlamaque pluton (Lac Herbin and Beaufor QTC veins). The Lamaque samples were selected from two different exploration zones, 2 km apart: the Triangle zone (Lamaque-T) and the Parallel zone (Lamaque-P).

2.2.1. Goldex

The Goldex mine is located 1.5 km north of the CLLFZ, in the southern part of the district. QTC veins and veinlets occur inside a 0.1–0.25 km by 3.8 km quartz-diorite intrusion in the metabasalts of the Jacola Formation (Genest, 2012). The mineralization was emplaced as centimeter-to-decimeter veins and veinlets in a complex stockwork system. Veins present proximal (± 0.5 m thick) albite and sericite-rich alteration haloes and a biotite-chlorite distal alteration halo 3–10 m thick (Genest, 2012). Sample 91 is from a quartz vein with disseminated tourmaline and pyrite in contact with a feldspathic and chlorite alteration. The sample was collected from a drill core in a stockwork vein system at 134 m depth (Fig. 2A).

2.2.2. Lamaque

The Triangle and Parallel zones are part of the Lamaque deposit, located in the southern part of the Val d'Or district. The well-know Sigma mine nearby represents the northern extension of the Lamaque deposit (Robert and Brown, 1986). Together, they produced over ten million oz of gold. The Triangle zone is located 2.5 km from the historical Lamaque mine. It has been an operational mine since March 2019 (Eldorado gold), with an average grade of 7 g/t Au (Beauregard et al., 2014). The Parallel zone is a current exploration project located 500 m from the Lamaque deposit and 2 km from the Triangle zone. QTC veins with disseminated pyrite occur in an 800 × 400 m dioritic intrusion in the andesite of the Val-d'Or Formation. Veins were emplaced in a series of sub-vertical shear zones and fractures, and also as extensional shear vein splays (Beauregard et al., 2014). Sample 85 is from a quartz-tourmaline vein with pyrite and chlorite. Sample 87 is from a quartz-tourmaline vein with pyrite and a larger proportion of chlorite and some K-feldspar veining. Samples 85 and 87 were collected from the same drill core in the Triangle zone, at 208.5 m and 211.5 m depths respectively (Fig. 2B and C). Sample 87 presents pervasive chlorite and a K-feldspar veinlets. Sample 88 represents quartz-tourmaline veins with disseminated pyrite, collected from the Parallel zonein a drill core at 212 m depth (Fig. 2D).

2.2.3. Lac Herbin

The Lac Herbin mine is located in the center of the 170 km^2 Bourlamaque pluton, which is dioritic to tonalitic in composition (Lemarchand, 2012). QTC veins emplaced in shear zones from less than 1 to 3.5 m width (Rezeau et al., 2017). Several deformed dioritic dykes crosscut the deposit parallel to the QTC veins. Sample 73 is a centimeter-wide quartz vein with a veinlet of sulfides and tourmaline veinlets. Parallel veinlets of tourmaline and pyrite-chalcopyrite are separated within the quartz vein (Fig. 2E). The sample was collected in the underground part of the mine, from an E-W trending shear zone at level 15.

2.2.4. Beaufor

The Beaufor mine is located in the eastern part of the Bourlamaque pluton. Quartz-tourmaline veins, with pyrite, chalcopyrite, and chlorite were emplaced in decimeter-to-meter lenses within subhorizontal tensional shears zones. The Beaufor deposit formed at the border of the Bourlamaque pluton and mafic rocks of the Dubuisson Formation. Sample 11 is from a quartz-tourmaline vein with pyrite, chalcopyrite, and chlorite, and was collected from a 2 m-wide crack-and-seal vein in the 22C-355 level of the underground mine (Fig. 2F).

3. Materials and methods

The three veins from Lamaque were samples from drill cores, and those from Goldex, Lac Herbin and Beaufor were hand samples. All were sampled inside the representative quartz vein and contain visible sulfides and tourmaline. Samples were crushed and sulfide minerals were separated by density from the lighter silicates using a hydroseparator. The heavy mineral assemblage, including gold and its alloys (Ag, Te) was characterized via SEM-EDX (Fig. 3) on isolated grains with a Hitachi S-3400 N type II (4 detectors) at 15 kV.

Representative tourmaline grains, ranging from 60 to 600 μm long, were handpicked from each sample under a binocular microscope and set in two epoxy mounts. Major, trace, and rare earth elements were measured on one sample mount, which contained 48 tourmaline grains-eight per sample. They were analyzed using a New wave 213 nm Nd-YAG laser ablation system coupled with an iCAP Qc ICP-MS at McGill University, Montréal, Canada. The 60 μm beam made a 10 μm deep ablation channel along the length of each tourmaline grain (between 70 and 300 μm) at 6 μm/s. The laser is operated continuously at 10 Hz and 65% energy. The energy of the laser is 0.244 mJ, with a flux of 8.63 J/cm2. The washing time of the laser is 40 s and heating time is 30 s. The instrumental mass fractionation and analytical quality were determined by repeat analysis of reference materials, NIST 160, NIST 612, and NIST 614.

Boron isotopes were measured on 76 representative tourmaline grains from the six samples, which were mounted in the second epoxy mount. The analysis was undertaken using the CAMECA 1280-HR secondary ion mass spectrometer (SIMS) at the German Research Centre for Geosciences (GFZ) in Potsdam, Germany (Table 2). The sample mount was cleaned and coated with high-purity gold before SIMS analyses. The instrument was tuned with a $^{16}O^-$ ion beam of ca. 3nA intensity, focused to a 5 μm spot on the sample surface. Secondary ions were measured in multi-collector mode using Faraday cups. For further analytical details of the tourmaline analysis carried out at GFZ using the 1280-HR instrument, see Lambert-Smith et al. (2016). The instrumental

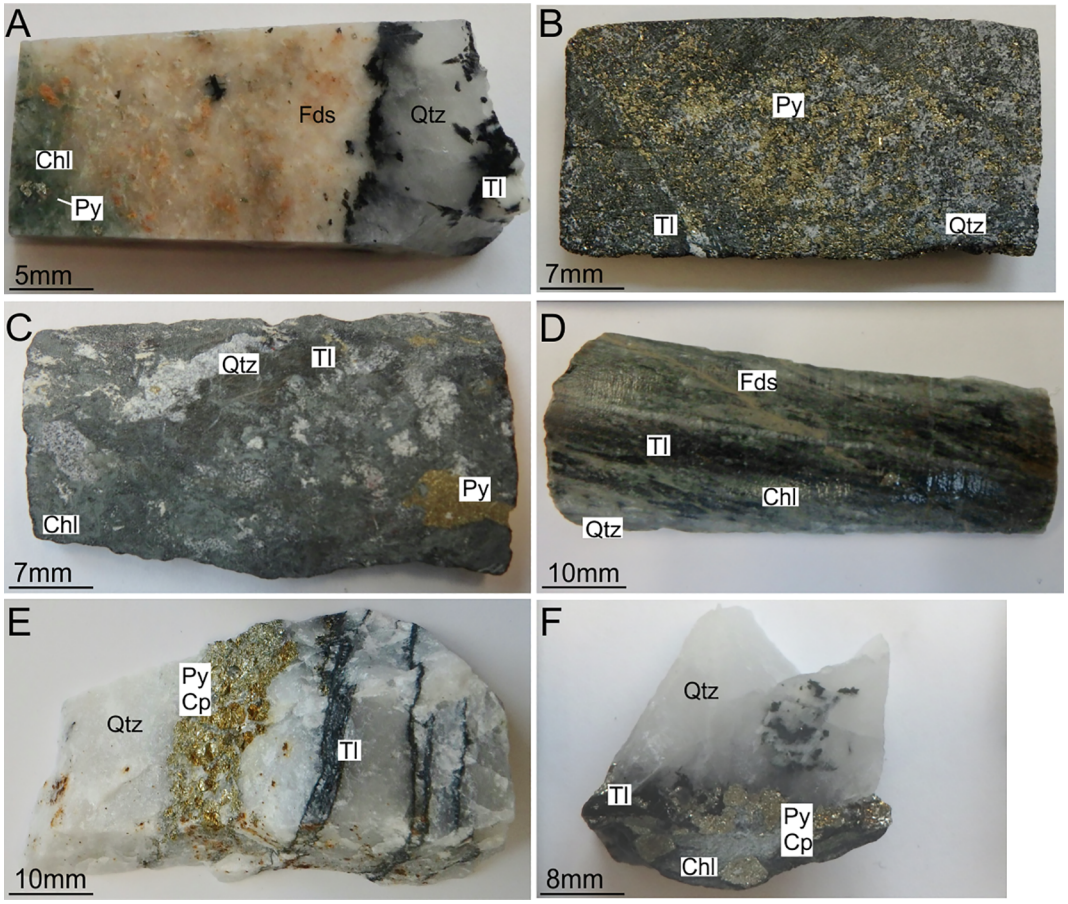

Fig. 2. Hand sample pictures of investigated vein samples. (A) quartz-tourmaline vein with pyrite, K-feldspar, and chlorite in sample 91 from a Goldex mine drill core, (B) quartz-tourmaline vein with disseminated pyrite in sample 88 from the Lamaque parallel exploration zone drill core, (C) quartz-tourmaline vein with pyrite and chlorite in sample 85, (D) quartz-tourmaline vein with chlorite and feldspar veinlets in sample 87 from the same Lamaque triangle exploration zone drill core, (E) quartz-tourmaline vein with pyrite and chalcopyrite from the Lac Herbin mine, and (F) quartz-tourmaline vein with pyrite, chalcopyrite, and chlorite from the Beaufor mine. Py = pyrite, Chl = chlorite, Fds = feldspath, Qtz = quartz, Tl = tourmaline, and Cp = chalcopyrite.

mass fractionation and analytical quality were determined by repeat analysis of tourmaline reference materials, Harvard 112,566 schorl and Harvard 108,796 dravite, which span the compositional range of the tourmalines studied here. Each analysis consisted of 20 measurements at the ^{10}B and ^{11}B mass stations, and the internal precision was typically 0.1‰ (1 s.d.). The repeatability determined from multiple analyses of the reference tourmalines during the analytic session was better than 0.3‰ individually (1 sd, n = 54). The overall repeatability calculated for both reference tourmalines together was 0.6‰ (1 sd), which includes any chemical matrix effect in the shorl-dravite composition range. Boron isotope ratios are reported in delta notation ($\delta^{11}B = (^{11}B/^{10}B)_{sample}/(^{11}B/^{10}B)_{std}$) in per mil (‰) relative to the NIST SRM 951 standard (Catanzaro et al., 1970).

Pyrite grains in thin-section were measured by laser-ablation ICPMS in element-mapping mode or Ag, As, Au, B, Ba, Co, Mg, Mo, Ni, and Pb. Five pyrite grains were mapped using a Resonetics S-155-LR with a 193 nm Excimer laser ablation system coupled to an Agilent 7700x quadrupole ICP-MS at the University of New Brunswick, Fredericton, Canada. The instrumental mass fractionation and analytical quality were determined by repeat analysis of reference materials NIST 610 and MASS1. Eight-to-10 μm-deep ablations were perform at a travel speed of 25 μm/s with a 36 μm-diameter beam. The analyzed pyrites grains were selected based on their size (> 5 mm) and the presence of visible zonation in reflected light observations. The selected grains represent the dominant grain morphology in the QTC veins from the Lac Herbin and Goldex deposits, as compared to less abundant, smaller, more idiomorphic cubic grains, which are late-stage and have no gold inclusions. Pyrites with a central pitted texture and smooth halo were found in thin-sections of the six samples and were analyzed.

4. Results

4.1. Mineralogy

The QTC veins contain a similar mineral assemblage in all of the samples, comprising quartz, carbonate, tourmaline, pyrite, K-feldspar, muscovite, chlorite ± pyrrhotite, chalcopyrite, molybdenite, and scheelite (Tables 1; Fig. 2). Pyrite is disseminated in the veins and ranges from a micrometer in size, and up to 1 cm wide in the samples. It can represent up to 10% of the vein mineral assemblage, either aggregated or more sporadic. Pyrite is the most abundant sulfide and is gold-bearing (Figs. 3 and 4), except for a later generation of smaller, idiomorphic cubic grains, which are barren. SEM-EDX measurements on pyrite indicate the presence of micro-inclusions of native gold or electrum. At the Lamaque deposit (the Triangle and Parallel deposits are described together), gold is frequently associated with tellurides, including calaverite ($AuTe_2$) and krennerite (Au_3AgTe_3). The Lac Herbin and Beaufor deposits also contain euhedral, Ni-Co-rich arsenopyrites.

Tourmaline occurs disseminated or in late veinlets within the QTC veins, and both were sampled for the study (Fig. 2). These tourmaline veinlets contain disseminated cubic pyrites with few gold inclusions on their surface caused by a late remobilzation. Despite the overall similarity in the mineralogy of the vein material from one deposit to

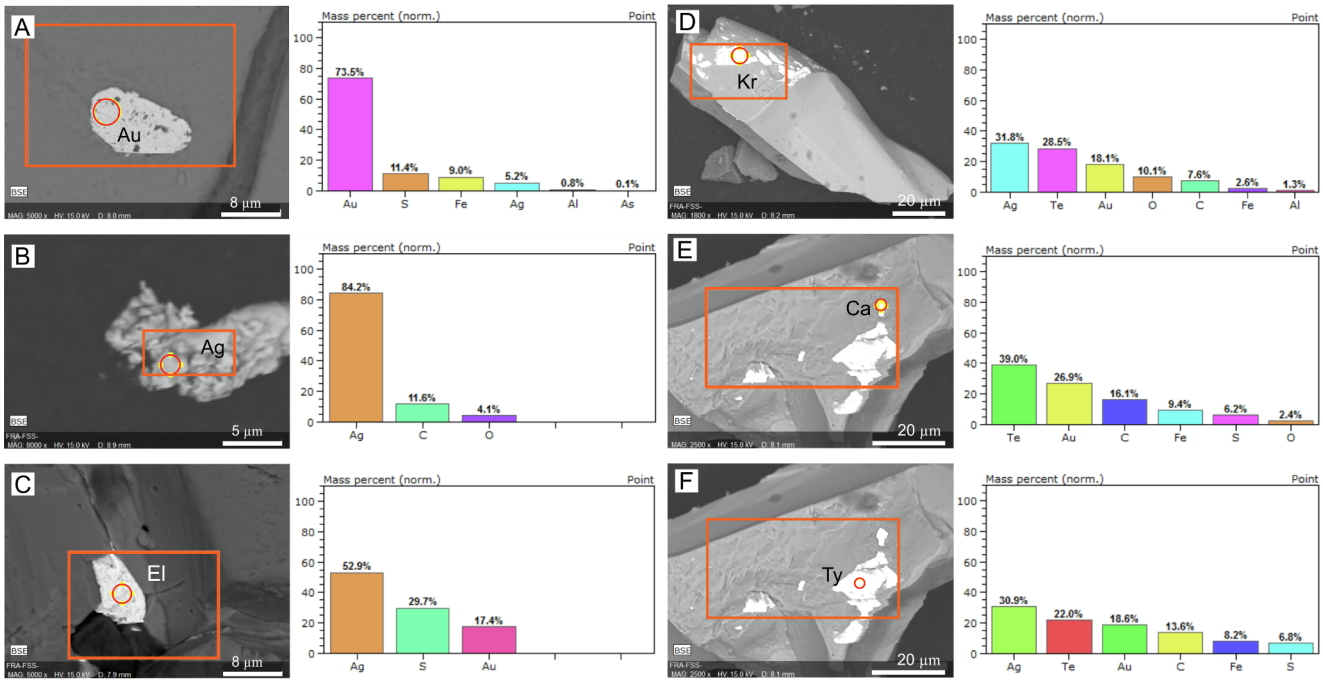

Fig. 3. BSE-SEM photomicrographs of regions analyzed by SEM-EDX from Val-d'Or deposit sample grains. The red circle indicates with precision the area analyzed. From Lamaque, analysis of A) gold (Au), B) native silver (Ag), C) electrum (Ag, Au), D) krennerite (Au_3AgTe_8) as inclusions in different pyrite grains, E) calaverite ($AuTe_2$), and F) tetradymite (Bi_2Te_2S) in inclusions in the same pyrite grain. The carbon content is related to the epoxy mounts which hold the grains. Sulfur and iron contents are related to the pyrite which hosts the inclusions. Au = gold, Ag = silver, El = electrum, Kr = krennerite, Ca = calaverite, and Ty = tetradymite. (For interpretation of the references to colour in this figure legend, the reader is referred to the web version of this article.)

another, there are slight differences in mineral proportions (Table 1). This variation is linked to a change from quartz to albite and microcline in the vein, particularly for quartz and carbonate, which represent ~50% of Goldex and Lamaque vein modal mineralogy and ~90% of Lac Herbin and Beaufor vein modal mineralogy. For all deposits sampled, tourmaline represents ~2% of the sample material. In some veins, tourmaline proportion can reach > 50% of the vein assemblage.

4.2. Element mapping in pyrites

Element mapping of pyrite in thin sections from the Lac Herbin and Goldex deposits gave consistent results regarding the pyrite paragenesis (Figs. 4 and 5). Mapping of Ag, As, Au, B, Ba, Co, Mg, Mo, Ni, and Pb enables different pyrite stages to be distinguished. Three observable geochemically distinct zones in the grains suggest three generations of pyrite growth (Figs. 4 and 5). The first generation of pyrite is in the crystal cores (Fig. 4A and 5A), with a ragged border (Pyrite 1). It contains numerous 10–30 µm inclusions, including gold and relatively Mg-rich phase too small for identification. The ragged border of Pyrite 1 indicates dissolution. The outer halo of this pyrite contains 250–200 µm diameter inclusions of B- and Ba-rich minerals, mainly tourmaline and barite (Fig. 4B and 5B). Pyrite 2 occurs as an overgrowth on Pyrite 1 and has a Co-rich composition (Fig. 4C and 5C). The composition of Pyrite 3 changes outward to an As- and Ni-rich composition with no further more association with gold (Fig. 4C and 5C). Pyrites 2 and 3 are inclusion-free. Where the grains showed late brittle deformation, gold and other metals (Ag, Mo, Pb) from pyrite cores (as inclusions or in the lattice) were remobilized into fractures and pores (Fig. 4D).

4.3. Major, trace and REE elements in tourmaline

The presence of tourmaline inclusions in Pyrite 1 suggests that tourmaline began to crystallize at the end of the Pyrite 1 formation. Tourmaline compositions on a district scale vary from a Mg-rich to an Fe-rich composition, as indicated by the Fe/Mg and Na/Ca plots (Fig. 6A). The northeastern deposits (Beaufor and Lac Herbin) are dravitic (Mg-rich) and the southwestern deposits (Goldex and Lamaque) are schorlitic (Fe-rich) tourmalines. However, tourmaline trace element contents show no systematic trends. The average primitive mantle-normalized trace element values (McDonough and Sun, 1995) are heterogeneous among the deposits (Fig. 6B; Table A1). Most show Pb and Sr enrichment and Ce depletion compared with neighboring trace-elements (Fig. 6B). In general, tourmaline from the Lamaque deposit has higher trace-element concentrations than those from the other deposits, especially for U, Nb, Pb, Zr, for the REE generally, and for the HREE in particular (Fig. 6B). Tourmaline in all of the deposits shows a positive Eu anomaly, but this is less marked in the Lamaque tourmaline than for the other deposits.

4.4. Boron isotopes in tourmaline

Boron isotope analysis resulted in $\delta^{11}B$ values ranging from −15.6 to −7.7‰ (Fig. 6C). Ten grains were typically analyzed from each deposit and the internal variations was found to be about 2–3‰ (Table 2). The B-isotope ratios from individual locations across the Val-d'Or district show a spatial pattern; the southwestern Goldex and Lamaque samples have lighter $\delta^{11}B$ values, from −15.6 to −9.1‰ whereas the Beaufor and Lac Herbin samples from farther east in the district yielded higher $\delta^{11}B$ values, from –11.2 to −7.7‰ (Fig. 7, Table 2). This apparently systematic increase in $\delta^{11}B$ values from west to east agrees with the results of an earlier study by Beaudoin et al., 2013.

5. Discussion

Two interpretations are possible for the proposed three-phase evolution of the Val-d'Or mineralization based on the pyrite paragenesis: (1) multiple fluid pulses during a single hydrothermal event (Robert, 1994), or (2) multiple, discontinuous hydrothermal episodes spread over a longer time span (Fontaine et al., 2017; Molnár et al., 2018). The

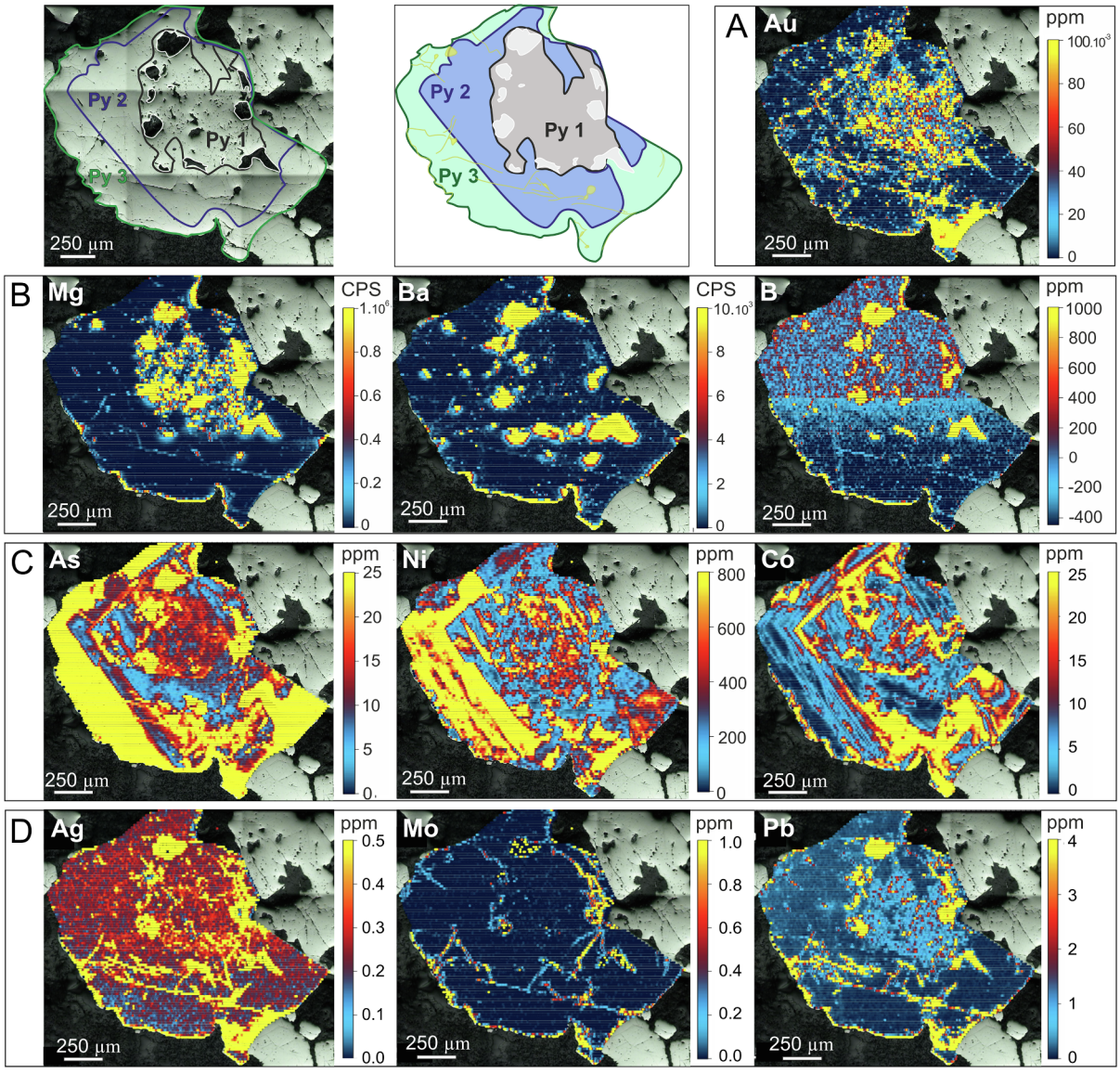

Fig. 4. Element mapping of Au, Mg, Ba, B, As, Ni, Co, Ag, Mo and Pb by LA-ICP-MS on polyphased pyrite grain from the Lac Herbin deposits. In the Lac Herbin pyrite, A) Au occurs as inclusions in the core and is remobilized in late fractures (Au accumulation at the bottom of Pyrite 3 is an effect of saturation in the fracture), B) while Mg is present only in the core in the inclusions. Ba and B are concentrated in inclusions at the margin of Pyrite 1 and 2, and in the dissolution halo of Pyrite 3. C) Pyrite 2 is Co-rich. As and Ni concentrations suggest a zoning pattern, which forms cubic Pyrites 2 and 3. Pyrite 3 is particularly As-Ni-rich. D) Ag, Mo, and Pb are concentrated in the fractures, indicating remobilization.

similar mineralogical signature of the veins suggests a common origin for the vein forming fluid. The pyrite element mapping helps to distinguish between evolution during one continuous hydrothermal event versus an episodic mineralization scenario. The first would be recorded in the pyrite as continuous crystallization (Murowchick and Barnes, 1987; Román et al., 2019), as is the case for the gradual variation between Pyrite 2 and Pyrite 3 (Fig. 4C and 5C). In contrast, the discontinuous growth and partial resorption between Pyrite 1 and Pyrite 2, suggests two distinct episodes in the vein field construction. This may be associated with episodic pulses of fluid rising through the CLLFZ fault system.

5.1. Phase 1

Phase 1 represents the beginning of vein formation with the first hydrothermal pulse. It crystallized the quartz-carbonate vein material and disseminated gold-bearing pyrite. The irregular shape of Pyrite 1, associated with abundant mineral inclusions and clustered pores, suggests fast crystallization and supersaturation conditions (Murowchick and Barnes, 1987; Wang et al., 2012; Román et al., 2019). The Au maps and SEM-EDX analysis indicate an uneven gold distribution between the samples which corroborates the uneven gold content distribution in the district (Robert et al., 2005). The gold content in the Sigma-Lamaque deposit is higher than that in the surrounding deposits in the Val-d'Or district (Robert et al., 2005). In veins from the Lamaque deposit, gold is found as an alloy with Ag, Pb, and Te. In the other studied deposits, gold is either native or is associated with silver (Table 1). This difference could be caused by a Te-Ag-Pb-rich fluid that was restricted at the scale of Sigma-Lamaque deposit, and therefore only impacted this deposit.

5.2. Phase 2

Phase 2 began with the crystallization of tourmaline and barite at the end of Pyrite 1. The occurrence of barite in the veins and the positive Eu anomaly recorded in the tourmalines indicate an oxidized

Table 1
Mineralogy of the Val-d'Or quartz-carbonate-tourmaline veins.

		Goldex	Lam. Parallel	Lam. Triangle	Lac H.	Beaufor
Pyrite Habit	Cubic Sub-euhedral Anhedral					
Metal inclusions in pyrite or isolated	Gold (Au) Silver (Ag) Electrum (Au, Ag)					
Tellurium	Tellurobismuthite (Bi_2Te_3) Calaverite ($AuTe_2$) Krennerite (Au_3AgTe_8) Tetradymite (Bi_2Te_2S)					
Tourmaline	Schorl Uvite Dravite					
Barite						
Sulfides	Pyrrhotite (Fe_7S_8) Chalcopyrite ($CuFeS_2$) Molybdenite (MoS) Arsenopyrite (FeAsS)					
Quartz						
Carbonate	Calcite Dolomie					
Feldspar	Albite Microcline (K-feldspar)					
Mica	Biotite Muscovite					
Titanite Schellite Chlorite Rutile Hematite Apatite						
Zircon						

Minor mineral in the assemblage Major mineral in the assemblage

> 50% of the assemblage

fluid as tourmaline-barite forming-fluid. The dissolution border of Pyrite 1 indicates a reaction with this tourmaline-barite forming-fluid. Barite is less abundant than tourmaline in the deposits, and was only observed as inclusions in Pyrite 1.

5.3. Phase 3

Phase 3 started with a new pulse of hydrothermal fluids, which enabled a return to reduced conditions and the precipitation of more pyrite. Pyrite 2 and 3 are not auriferous. Pyrite 2 is Co-rich and Pyrite 3 is As-Ni-rich compared with Pyrite 1 (Fig. 4C and 5C). The homogenous distribution of Co, As and Ni in Pyrites 2 and 3 indicates that the Co, As, and Ni is structurally bound with the pyrite. Pyrite 2 and 3 show Co-rich and As-Ni-rich zonation patterns respectively, and are inclusion-free. Arsenic, nickel, and cobalt were introduced either during or after the oxidized phase (Phase 2), with the Phase 3 hydrothermal fluid pulse. Ni-Co-rich arsenopyrite also formed during phase 3. The pyrite zonation pattern suggests slow crystallization kinetics, under low-boiling (gradual cooling and physico-chemical variation) or non-boiling conditions in a less-sulfide-saturated environment (Murowchick and Barnes, 1987; Román et al., 2019) compared to Phase 1. Tourmaline continued to continuously crystallize with Pyrite 2 and Pyrite 3, with a

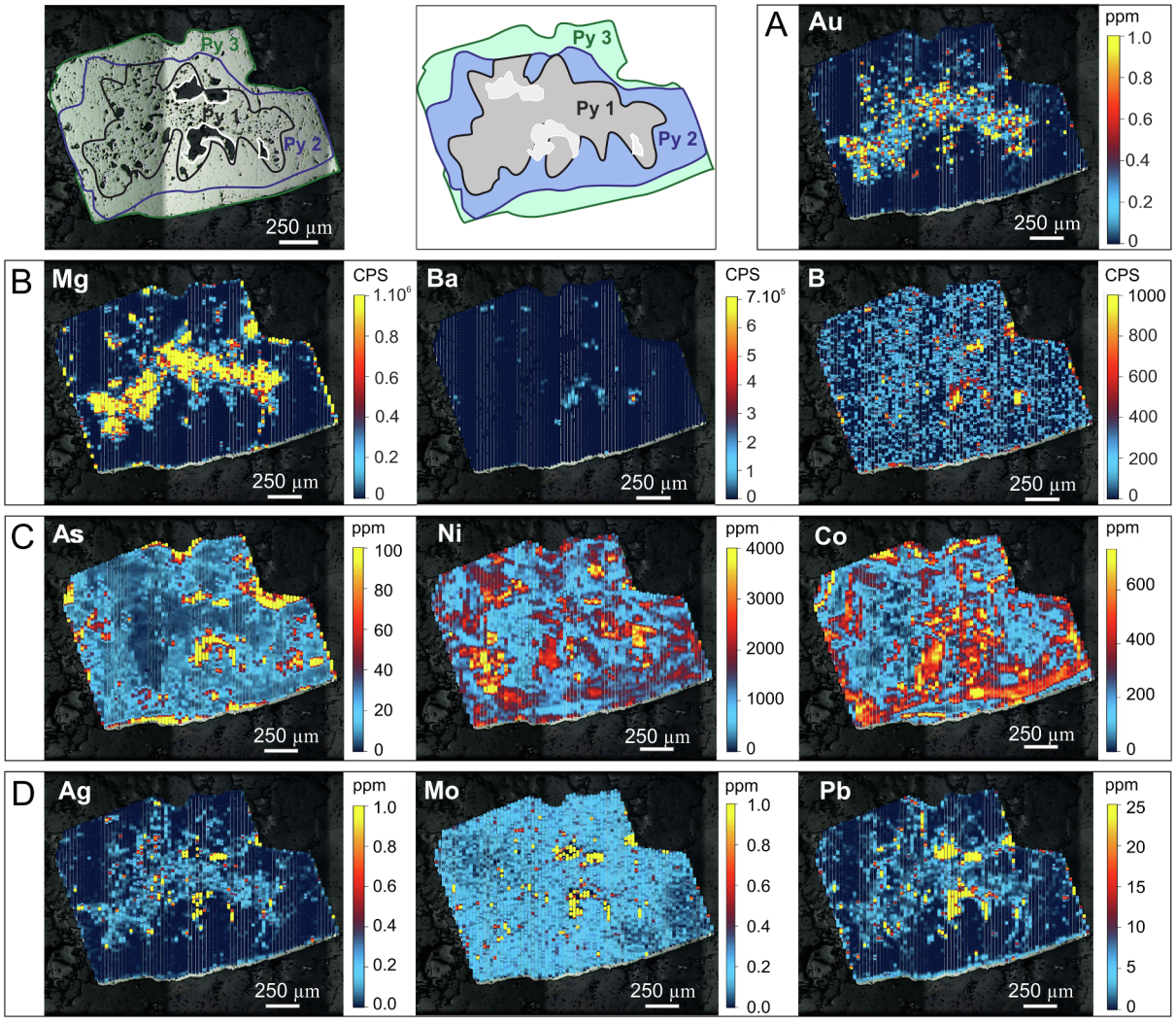

Fig. 5. Element mapping of Au, Mg, Ba, B, As, Ni, Co, Ag, Mo, and Pb by LA-ICP-MS on polyphased pyrite grain from Goldex deposits. The white rim represents the edge of the pyrite. In the Goldex pyrite, A) Au and B) Mg are concentrated in micro-inclusions in the core of Pyrite 1. Au concentrations reach 1 ppm. B) Ba and B are more important than in the Lac Herbin pyrite, and are concentrated in inclusions in the Pyrite 1 dissolution halo, at the outer grain boundary.C) Pyrite 2 is Co-rich. As and Ni concentrations are higher than in Lac Herbin pyrite and also suggest a zoning pattern in the outer part of the pyrite, indicating Pyrite 3 (As-rich). D) There is no indication of fracture and metal remobilization.

late mineral assemblage (muscovite, rutile, titanite; Kerrich and King, 1993). After the last pyrite overgrowth (Pyrite 3), pyrite fracturing and destabilization enabled the remobilization of gold and metals (Ag, Mo, Pb) into these fractures from the core (Pyrite 1) to the edges (Pyrite 3) and more rarely on the irregular surfaces of the cubic pyrite formed during Phase 3. This remobilization followed a late deformation of the region, probably Proterozoic, impacting the deposits, but not necessarily uniformly (Zhang et al., 2014b). The Lac Herbin pyrite indicates remobilization, but fracturing is not observed in Goldex pyrite. This late remobilization at grain scale may account for the nuggety gold distribution observed in the deposits (Bonnemaison and Marcoux, 1990).

5.4. The three-stage evolution

We propose that each phase represents a particular redox environment, and that each pyrite growth stage (Pyrite 1, 2, and 3) represents a hydrothermal fluid pulse event (Fig. 8). Pyrite 1 formed during Phase 1 and the beginning of Phase 2. Phase 2 began with the formation of tourmaline and barite. Phase 3 then formed Pyrite 2, Pyrite 3, and tourmaline (barite only cristallized during Phase 2). Independent evidence for the three model is the observation that quartz in the QTC veins at the Lac Herbin deposit contains three types of successively-tapped fluid inclusions (Rezeau et al., 2017): an early gold-bearing aqueous-carbonic fluid, a barren high-temperature moderately-saline aqueous fluid, and a barren low-temperature saline aqueous fluid. The first, gold-bearing fluid of Rezeau et al. (2017) corresponds to Phase 1, while the second, barren high-temperature fluid saline aqueous fluids, which would have remobilized gold in late fractures corresponding to the end of our Phase 3. The final, low-temperature fluid, is not recorded in the pyrite growth zones, and could be Proterozoic (Boullier et al., 1998).

5.5. Tourmaline B-isotope variations and implications for fluid source

The $\delta^{11}B$ values of tourmaline from all samples vary between −15.6‰ to −7.7‰, but the variation within a single deposit is on the order of 2–3‰ (Fig. 6C; Fig. 7). This narrow range is similar to results from a previous boron study in the district (Beaudoin et al., 2013) but could be related to the small number of samples in this study (one per deposit and three for Lamaque). The Lamaque tourmalines are the exception in terms of a larger number of sample (n = 3) and a larger range of values, from −14 to −9.1‰, while tourmaline from the Sigma

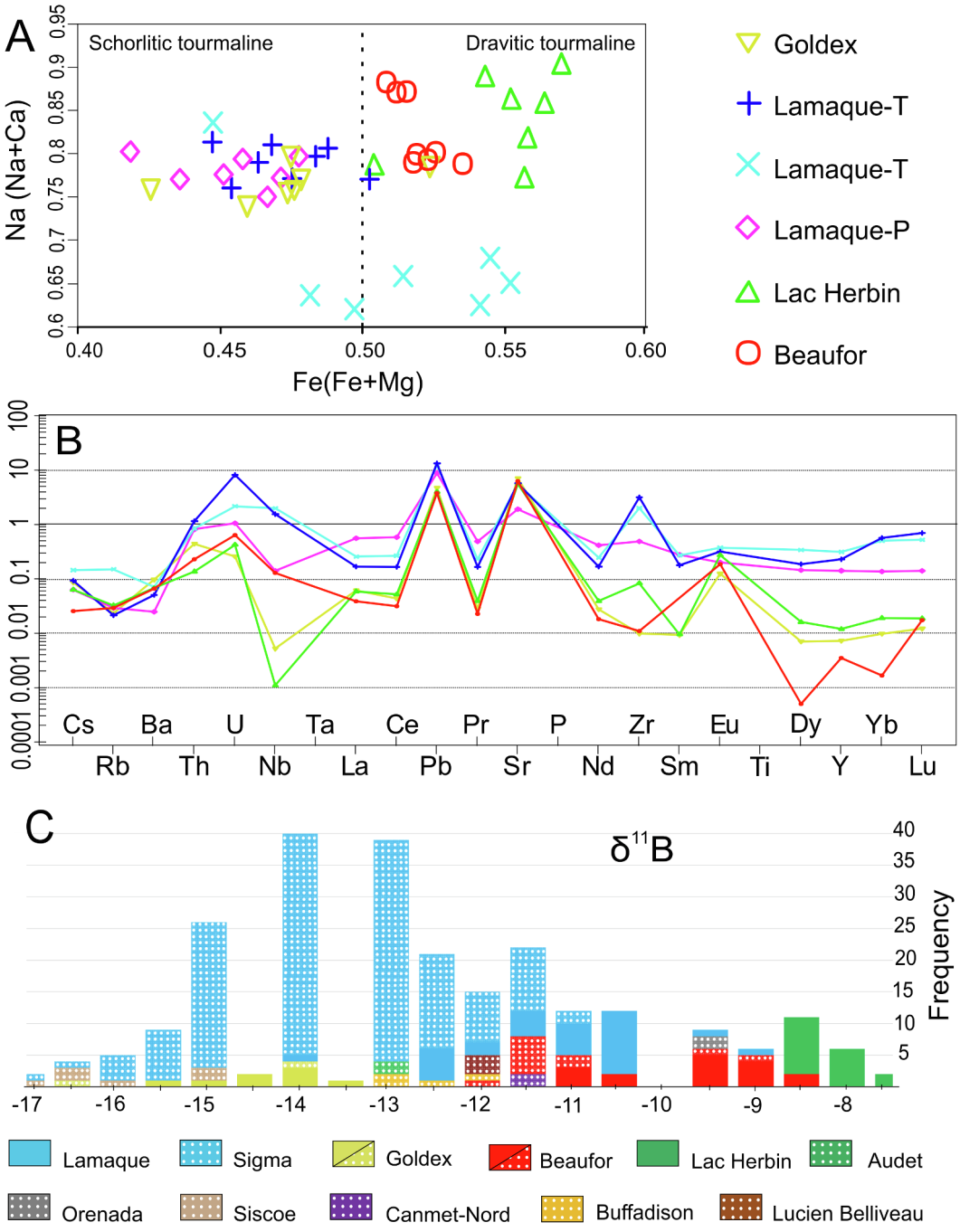

Fig. 6. Geochemical analyses of select Val-d'Or tourmalines. A) Mg/(Fe + Mg) vs. Na/(Na + Ca) variations in Val-d'Or tourmaline, with schorl-dravite nomenclature. B) Val-d'Or tourmaline average trace element compositions plotted on a primitive mantle-normalized diagram (mantle values from McDonough and Sun (1995)). C) Val-d'Or tourmaline $\delta^{11}B$ values in ‰ (analytical error is ± 0.6‰, 1 sd). The dotted bars are values from Beaudoin et al. (2013). For the Lamaque deposit, the $\delta^{11}B$ values combine data from the Triangle and Parallel zone samples. Sigma and Lamaque deposits are geographically close and geochemically related. The Audet deposit shares the same structure as the Lac Herbin deposit.

deposit also yield a considerable range of $\delta^{11}B$ values, from −16.4 to −10.7‰ (Beaudoin et al., 2013). Beaudoin et al. (2013) suggested that the large range $\delta^{11}B$ values at the Sigma deposit is caused by repetitive closed-reservoir tourmaline precipitation with a Rayleigh fractionation, followed by vein re-opening and the influx of new hydrothermal fluids during fault-valve cycles.

The $\delta^{11}B$ values suggest a spatial variation that divides the district into a southwest group (Goldex and Lamaque), with values from −15.6 to −11.6‰, and a northeast group (Lac Herbin and Beaufor), with a higher range of $\delta^{11}B$ from −11.2 to −7.7‰ (Fig. 7). This divide in the district corresponds to a difference in the tourmaline Fe/Mg ratio, although, on the grain scale, the boron isotope composition is largely independent of the tourmaline chemical composition (this study and Beaudoin et al., 2013). Tourmaline $\delta^{11}B$ values from Beaudoin et al. (2013) show the same spatial variation, with a southwest group (Sisco, Sigma, Audet, and Goldex) ranging between −15.5 to −11.6‰, and a northeast group (Orenada, Lucien Belliveau, Camnet-Nord, Buffadison, and Beaufor), with −12 to −9.5‰ (Fig. 6C). The highest $\delta^{11}B$ values (-9.5 to −7.7‰) are found close to large intrusions, such as Bourlamaque and the East Sullivan pluton (Fig. 7), but other locations in the eastern group also have high and are metavolcanic rocks (Lucien Béliveau and Buffadison). Futhermore, there are volcanic-hosted locations

Table 2
Summary of SIMS B-isotope analyses of select tourmalines.

Analysis	$^{11}B/^{10}B$ (meas.)	int. precision*	$^{11}B/^{10}B$ (corr.)**	$\delta^{11}B$***
Beaufor tourmalines from one sample				
Beaufor 1	3.925	0.13	4.0067	−9.1
Beaufor 2	3.9259	0.1	4.0076	−8.9
Beaufor 3	3.9261	0.1	4.0078	−8.9
Beaufor 4	3.9235	0.12	4.0051	−9.5
Beaufor 5	3.9239	0.12	4.0055	−9.4
Beaufor 6	3.9175	0.12	3.999	−11
Beaufor 7	3.9173	0.16	3.9987	−11.1
Beaufor 8	3.9231	0.1	4.0047	−9.6
Beaufor 9	3.9243	0.11	4.0059	−9.3
Beaufor 10	3.9229	0.09	4.0045	−9.7
Beaufor 11	3.923	0.13	4.0046	−9.6
Beaufor 12	3.924	0.12	4.0056	−9.4
Beaufor 13	3.918	0.15	3.9995	−10.9
Beaufor 14	3.9168	0.15	3.9983	−11.2
Beaufor 15	3.9195	0.15	4.001	−10.5
Beaufor 16	3.9228	0.16	4.0044	−9.7
Beaufor 19 05	3.8293	0.21	3.9993	−10.9
			Mean	**−9.9**
			St. dev.	**0.7**
Lac Herbin tourmalines from one sample				
LacHerbin 1	3.9276	0.1	4.0093	−8.5
LacHerbin 2	3.9294	0.09	4.0112	−8,0
LacHerbin 3	3.9297	0.09	4.0114	−8,0
LacHerbin 4	3.9276	0.1	4.0093	−8.5
LacHerbin 5	3.9243	0.09	4.0059	−9.3
LacHerbin 6	3.9275	0.12	4.0091	−8.5
LacHerbin 7	3.9271	0.14	4.0088	−8.6
LacHerbin 8	3.9272	0.1	4.0089	−8.6
LacHerbin 9	3.9299	0.13	4.0116	−7.9
LacHerbin 10	3.9257	0.13	4.0073	−9,0
LacHerbin 11	3.9307	0.12	4.0125	−7.7
LacHerbin 12	3.9273	0.1	4.0089	−8.6
LacHerbin 13	3.928	0.14	4.0097	−8.4
LacHerbin 14	3.928	0.07	4.0097	−8.4
LacHerbin 15	3.9257	0.13	4.0073	−9,0
LacHerbin 16	3.9265	0.16	4.0082	−8.8
LacHerbin 17	3.9289	0.11	4.0106	−8.2
LacHerbin 18	3.9281	0.12	4.0098	−8.4
LacHerbin 19	3.9272	0.12	4.0089	−8.6
LacHerbin 20	3.9248	0.13	4.0064	−9.2
LacHerbin 21	3.9277	0.11	4.0094	−8.5
			Mean	**−8.5**
			St. dev.	**0.4**
Lamaque Triangle tourmalines from two samples				
85 Lamaque 1	3.8366	0.2	4.0069	−9.1
85 Lamaque 2	3.8252	0.15	3.995	−12,0
85 Lamaque 3	3.8268	0.18	3.9967	−11.6
85 Lamaque 4	3.8285	0.16	3.9985	−11.2
85 Lamaque 5	3.8238	0.16	3.9935	−12.4
85 Lamaque 9	3.8286	0.2	3.9986	−11.1
85 Lamaque 8	3.8294	0.18	3.9994	−10.9
85 Lamaque 7	3.8306	0.24	4.0007	−10.6
85 Lamaque 6	3.8296	0.19	3.9997	−10.9
85 Lamaque 10	3.8325	0.17	4.0026	−10.1
85 Lamaque 11	3.8347	0.18	4.0049	−9.6
			Mean	**−10.8**
			St. dev.	**0.9**
87 Lamaque 1	3.8278	0.17	3.9977	−11.3
87 Lamaque 2	3.8305	0.19	4.0006	−10.6
87 Lamaque 3	3.8307	0.15	4.0007	−10.6
87 Lamaque 4	3.8263	0.16	3.9962	−11.7
87 Lamaque 5	3.8298	0.15	3.9999	−10.8
87 Lamaque 6	3.8284	0.13	3.9984	−11.2
87 Lamaque 7	3.8299	0.27	3.9999	−10.8
87 Lamaque 8	3.8298	0.21	3.9998	−10.8
87 Lamaque 9	3.8293	0.17	3.9993	−11,0
87 Lamaque 10	3.8296	0.17	3.9996	−10.9
			Mean	**−10.9**
			St. dev.	**0.3**

Table 2 (*continued*)

Analysis	$^{11}B/^{10}B$ (meas.)	int. precision*	$^{11}B/^{10}B$ (corr.)**	$\delta^{11}B$***
Lamaque Parallel tourmaline from one sample				
88 Lamaque 1	3.823	0.18	3.9928	−12.6
88 Lamaque 2	3.8232	0.19	3.9929	−12.5
88 Lamaque 3	3.8175	0.16	3.987	−14,0
88 Lamaque 4	3.8269	0.22	3.9968	−11.6
88 Lamaque 5	3.8227	0.12	3.9924	−12.7
88 Lamaque 6	3.8234	0.18	3.9932	−12.5
88 Lamaque 7	3.826	0.22	3.9958	−11.8
88 Lamaque 8	3.8229	0.21	3.9926	−12.6
			Mean	**−12.5**
			St. dev.	**0.6**
Goldex tourmalines from one sample				
91 Goldex 1	3.8115	0.16	3.9807	−15.6
91 Goldex 2	3.8141	0.21	3.9834	−14.9
91 Goldex 3	3.8177	0.16	3.9872	−13.9
91 Goldex 4	3.8144	0.15	3.9837	−14.8
91 Goldex 5	3.8135	0.19	3.9828	−15.1
91 Goldex 6	3.8161	0.14	3.9855	−14.4
91 Goldex 8	3.8173	0.14	3.9868	−14.1
91 Goldex 7	3.816	0.17	3.9855	−14.4
			Mean	**−14.6**
			St. dev.	**0.5**

Each analysis is on a different tourmaline grain.
*Internal precision of 20 measurements of $^{11}B/^{10}B$ in ‰ (1 s.d. / mean*1000).
**Corrected for instrument fractionation based on tourmaline reference materials.
*** Values in ‰ relative to NIST SRM 951 (4.04362: Catanzaro et al. (1970)).

in the southwestern (Goldex, Sisco) with low $\delta^{11}B$ values (Fig. 7), so the nature of the host rocks does not exert a controlling influence.

In terms of boron reservoirs, the B-isotope values reported are too low to be compatible with an unmodified marine source ($\delta^{11}B > 0$‰; Chaussidon and Appel, 1997; Marschall and Jiang, 2011) or a subducting slab (from −5‰ to +28‰; Marschall et al., 2009, Marocchi et al., 2011). The B-isotope range is instead consistent with, but not diagnostic of, a greenstone source (i.e., MORB at −7 ± 1‰; Marschall et al., 2017), with I-type intermediate magmas (−2 ± 5‰; Trumbull and Slack, 2018) or with clastic metamorphic rocks (prograde metamorphic tourmaline: −17‰ to +3‰, see Swihart and Moore, 1989; Jiang et al., 2002). In any case, the observed ± 8‰ range observed in Val-d'Or tourmaline cannot be explained by any one source type, and so requires a mixed fluid scenario, which is supported by the evidence of the discontinuous pyrite growth described above.

O-isotope thermometry from quartz-tourmaline pairs in the QTC veins at the Lamaque-Sigma deposit indicates a range of mineralization temperatures, ranging from approximately 350 to 450 °C (Beaudoin and Pitre, 2005). Over this 100° C range, the tourmaline-fluid fractionation factors vary by about 1‰ (-3.2‰ and −2.3‰, resp.; using Meyer et al., 2008), so the temperature effect on B isotope values is expected to be minor. Beaudoin and Pitre (2005) excluded temperature variations from explaining regional variations in $\delta^{18}O$, and proposed the contribution of more than one fluid with an average temperature of 350 °C for the QTC veins. The calculated $\delta^{11}B$ range of hydrothermal fluids is approximately −12.4‰ to −4.5‰ (fractionation factors from Meyer et al., 2008) which is supported by these new B-isotope values and those reported by Beaudoin et al. (2013). O-C–H and Sr- isotope ratios of the QTC veins suggest formation from a mixed fluid composed of two components: a prograde metamorphic fluid or a fluid thoroughly equilibrated with the metasedimentary and metavolcanic basement (Fluid 1), and a second fluid (Fluid 2) of supracrustal origin, with a possible marine source, trapped in pores and fractures (Beaudoin and Pitre, 2005; Beaudoin and Chiaradia, 2016). It is important to note that the $\delta^{18}O_{quartz}$ values from the Val-d'Or deposits are homogeneous within 11.5 ± 2.3‰ in the district, which suggests a decoupling of the

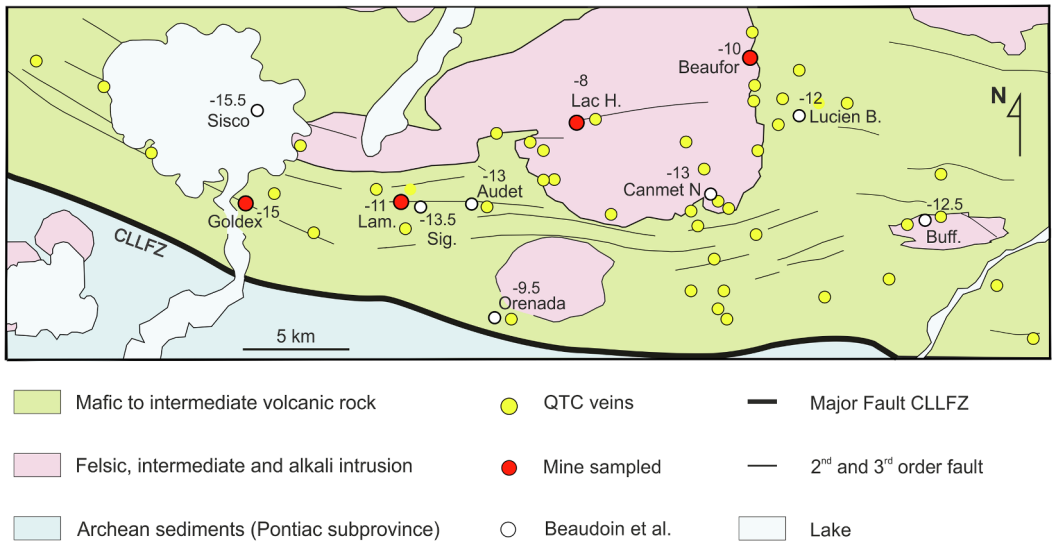

Fig. 7. Regional variation in average $\delta^{11}B$ values in ‰ for QTC vein tourmalines. Red dots represent locations corresponding with boron isotope analysis from this study and white dots represent those from Beaudoin et al. (2013). Lam. = Lamaque, Sig. = Sigma, Lucien B. = Lucien Belliveau, and Buff. = Buffadison. (For interpretation of the references to colour in this figure legend, the reader is referred to the web version of this article.)

boron and oxygen isotope systematics. These $\delta^{18}O_{quartz}$ values were attributed to a deep-seated metamorphic fluid source (Beaudoin and Pitre, 2005; Beaudoin and Chiaradia, 2016).

Our results support a metamorphic fluid source, and can be explained by a hydrothermal pulse of deep-seated metamorphic fluid (Fluid 1) that rose into the fault system and infiltrated a shallow crustal portion already saturated by an oxidized, B-bearing supracrustal fluid (Fluid 2). This oxidized B-bearing fluid is recorded by the occurance of barite and a positive Eu anomaly in coexisting tourmaline. At the end of the hydrothermal pulse (Fluid 1), the barren supracrustal fluid became dominant. It changed the redox condition of the environment and, for still unknown reason, stopped gold mineralization (Phase 2). This supracrustal fluid (Fluid 2) could be an evolved metamorphic fluid, which would have interacted with B- and Ba-rich lithologies, such as metasediments, during its rising in the CLLFZ, or a saline supracrustal fluid in the fault system. The $\delta^{11}B$ fluid values of approximately −12 to

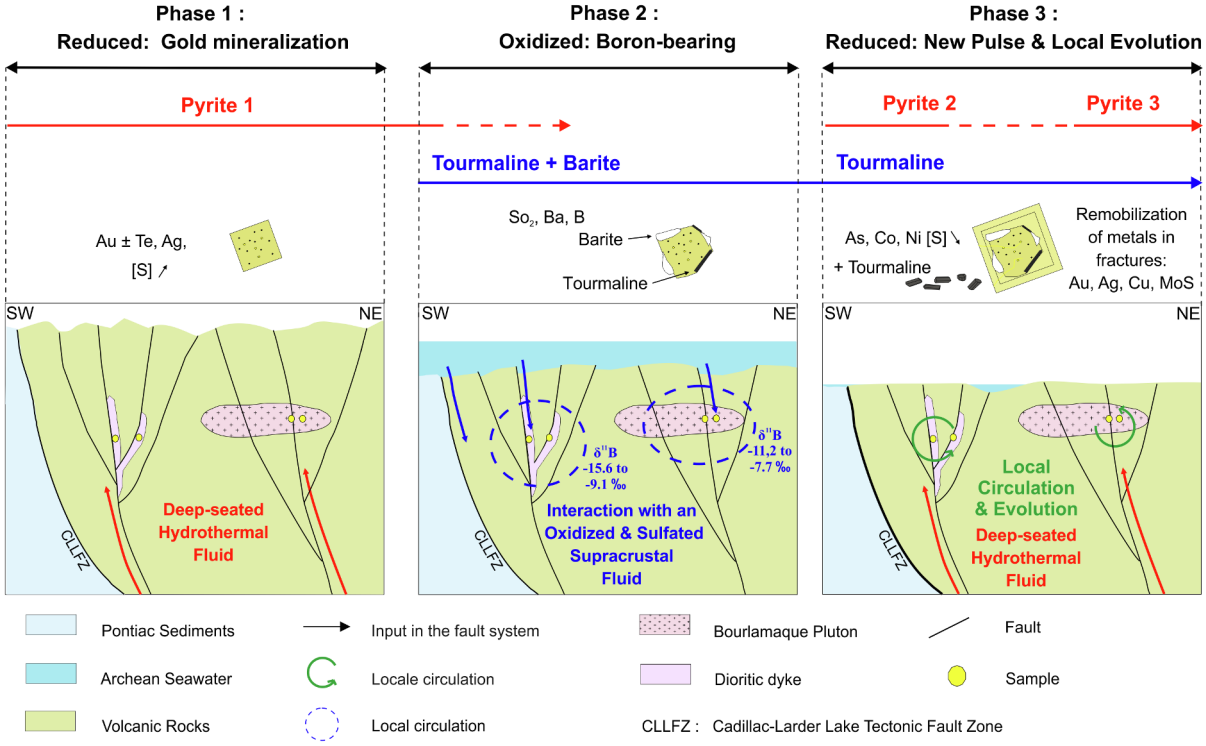

Fig. 8. Suggested scenario for quartz-tourmaline-carbonate vein evolution. Phase 1 represents the formation of gold-bearing pyrite from a deep-seated fluid under reducing conditions. Phase 2 involves mixing with an oxidized and supracrustal fluid, indicated by the dissolution of pyrite and the crystallization of barite and tourmaline. Phase 3 corresponds to a return to reducing conditions with the formation of non-auriferous As-Co-Ni-rich cubic pyrite, arsenopyrite, and tourmaline. Yellow circles represent the locations of the sampled QTC veins. (For interpretation of the references to colour in this figure legend, the reader is referred to the web version of this article.)

−6‰ are consistent with a prograde metamorphic fluid from metasedimentary and metavolcanic rocks. The higher $\delta^{11}B$ fluid values may be explained by mixing with a second fluid. A marine-derived pore fluid, as suggested by earlier studies, would be an excellent source of boron and sulfate, and consistent with the formation of barite and tourmaline. Contemporary to the QTC veins, the marine water source could be linked to the Timiskaming assemblage at 2678–2672 Ma (Davis, 2002). However, even the highest $\delta^{11}B$ fluid value, of −4.5‰, is too low for an unmodified marine-sourced fluid. The original B-isotope composition of pore fluid could be modified by later processes related to diagenesis and metamorphism, but a shift of approximately 20‰ would require very extensive exchange with boron in the host rocks. The other, perhaps more likely, hypothesis is that the end-member marine B-isotope signature of Fluid 2 was diluted in the mixed fluid. All that can be concluded with confidence is that isotopically light and heavy fluids contributed to the hydrothermal fluid from which the tourmaline formed. If one fluid had a marine origin, the B-isotope data require that its $\delta^{11}B$ signature was then modified by extensive exchange with the host rock or that it was diluted by the dominant, isotopically lighter, metamorphic fluid.

Concerning the spatial variation, the B-isotope values suggest a difference in fluid proportions in the different parts of the district, which could be caused by varying proximity to the main or subsidiary fault zones that control the hydrodynamics of the system (Beaudoin and Pitre, 2005). Depending on a deposit's location in the district, tourmaline and barite could have formed early in the vein system.

6. Conclusions

The Val-d'Or mining district remains a key example for understanding of orogenic gold deposit formation processes. The QTC veins across the district resulted from a multi-stage hydrothermal event that took place over a maximum 114 Ma period, between 2680 Ma (Wong et al., 1991) and 2566 ± 71 Ma (Olivo et al., 2007), after the end of the Superior Province accretion (Fig. 8). These results support a three-stage evolution for the QTC vein field. In Phase 1, gold mineralization took place early in the QTC vein field formation, in the third-order faults of the CLLFZ. Gold formed during the first hydrothermal pulse, forming disseminated inclusions in the pyrite, alloyed with variable proportions of silver and tellurium, and also as pure gold inclusions. This first fluid pulse involved deep-seated, reduced metamorphic fluids that infiltrated into a shallow crustal segment that was already saturated with an oxidized B-bearing supracrustal fluid. In Phase 2, the waning of the deep-seated fluid pulse enabled the supracrustal fluid to become dominant and this produced a change in the redox conditions, from reduced to oxidized, caused the precipitation of tourmaline and barite, and ended gold mineralization. This supracrustal fluid impacted the entire district, but mixing ratios varying with depth, location in the district, and the interaction time. The different mixing ratios are recorded by variability in the $\delta^{11}B$ signature of in tourmaline, which range from −15.6‰ to −7.7‰. The mixing ratio and B isotopic variation are not related to the host rock, but rather to their proximity to the main or subsidiary fault zones. Phase 3 involved a new pulse of reduced hydrothermal fluid and/or a decreased proportion of the supracrustal fluid, resulting in a change of fluid conditions from oxidized to reduced. Non-auriferous pyrite crystallized around Pyrite 1, tourmaline and barite, with a slower growth rate and Co-As-Ni-rich zonation (Pyrite 2 and 3). Tourmaline crystallization continued in those veins with pyrite and quartz but without barite. This three-stage evolution of the Val-d'Or vein field, with the mixing of deep-seated and supracrustal fluids, provides a new perspective to understand polyphase orogenic gold deposits worldwide.

Acknowledgments

We are grateful to the FRQNT and NSERC for the funding of this project. We thank Frederic Couffignal for expert assistance with the SIMS analysis at GFZ and Brandon Boucher for element mapping analysis. Reynald Lapointe, Christian Sasseville, and Anna Jung are thanked for their technical help. Thanks also to Stéphane de Souza and Vincent Van Hinsberg for their helpful comments and discussions during this work, and to Daniele Pinti for his great help in comments and suggestions to improve the manuscript. We thank the reviewers for their very constructive feedback.

Appendix A. Supplementary data

Supplementary data to this article can be found online at https://doi.org/10.1016/j.oregeorev.2020.103449.

References

Beaudoin, G., Pitre, D., 2005. Stable isotope geochemistry of the Archean Val-d'Or (Canada) orogenic gold vein field. Miner. Deposita 40, 59–75.
Beaudoin G., Rollion-Bard, C., and Giuliani, G., 2013, The boron isotope composition of tourmaline from the Val-d'Or orogenic gold deposits, Québec, Canada. Mineral Deposit Research For A High-Tech World. 12th SGA Biennial Meeting, Proceedings, v. 3, p. 1090-1092.
Beaudoin, G., Chiaradia, M., 2016. Fluid mixing in orogenic gold deposits: Evidence from the HO-Sr isotope composition of the Val-d'Or vein field, Abitibi, Canada. Chem. Geol. 437, 7–18.
Beauregard, A.J., Gaudreault, D., D'Amours, C., 2014. NI 43 101 Technical Report on the Lamaque property. Technical report prepared by Geologica Groupe-Conseil Inc. for Integra Gold Corp. 101, pages.
Bonnemaison, M., Marcoux, E., 1990. Auriferous mineralization in some shear-zones: A three-stage model of metallogenesis. Miner. Deposita 25 (2), 96–104.
Boullier, A.M., Robert, F., 1992. Palaeoseismic events recorded in Archean gold-quartz vein network, Val-d'Or, Abitibi, Quebec. Canada. Journal of Structural Geology 14 (2), 161–179.
Boullier, A.M., Firdaous, K., Robert, F., 1998. On the significance of aqueous fluid inclusions in gold-bearing quartz vein deposits from the southeastern Abitibi subprovince (Quebec, Canada). Econ. Geol. 93 (2), 216–223.
Card, K. D., & Ciesielski, A., 1986, DNAG# 1. Subdivisions of the Superior province of the Canadian shield. Geoscience Canada, v.13(1).
Catanzaro, E.J., Champion, C., Garner, E., Marinenko, G., Sappenfield, K., Shields, W., 1970. Boric acid: isotopic and assay standard reference materials. National Bureau of Standards (US), Special. Publication 260, 70.
Chaussidon, M., Appel, P.W.U., 1997. Boron isotopic composition of tourmalines from 3.8-Ga-old Isua supreacrustals, West Greenland: implication of the $\delta^{11}B$ value of early Archean seawater. Chem. Geol. v. 136(3–4), 171–180.
Couture, J.F., Pilote, P., Machado, N., Desrochers, J.P., 1994. Timing of gold mineralization in the Val-d'Or District, southern Abitibi Belt; evidence for two distinct mineralizing events. Econ. Geol. 89 (7), 1542–1551.
Davis, D.W., 2002. U-Pb geochronology of Archean metasedimentary rocks in the Pontiac and Abitibi subprovinces, Quebec, constraints on timing, provenance and regional tectonics. Precambr. Res. 115 (1–4), 97–117.
Dutrow, B.L., Henry, D.J., 2011. Tourmaline: a geologic DVD. Elements v. 7(5), 301–306.
Feng, R., Kerrich, R., 1992. Geochemical evolution of granitoids from the Archean Abitibi Southern Volcanic Zone and the Pontiac subprovince. Superior Province, Canada: implications for tectonic history and source regions: Chemical Geology 98 (1–2), 23–70.
Fontaine, A., Eglinger, A., Ada, K., André-Mayer, A.S., Reisberg, L., Siebenaller, L., Poujol, M., 2017. Geology of the world-class Kiaka polyphase gold deposit, West African Craton, Burkina Faso. J. Afr. Earth Sc. 126, 96–122.
Gaboury, D., 1999. Origine volcanogène des veines aurifères riches en sulfures de la mine Géant Dormant. Université du Québec à Chicoutimi, Abitibi, Québec.
Genest, R., 2012. Technical Report on the Estimation of the Mineral Resources at Goldex Mine, Quebec, Canada as at December 31, 2011. 102p.
Goldfarb, R.J., Groves, D.I., 2015. Orogenic gold: Common or evolving fluid and metal sources through time. Lithos 233, 2–26.
Green, A.G., Milkereit, B., Mayrand, L.J., Ludden, J.N., Hubert, C., Jackson, S.L., Simard, A., 1990. Deep structure of an Archean greenstone terrane. Nature v. 344(6264), 327.
Hanes, J.A., Archibald, D.A., Hodgson, C.J., Robert, F., 1992. Dating Archean auriferous quartz vein deposits in the Abitibi greenstone belt, Canada: $^{40}Ar/^{39}Ar$ evidence for a 70- to 100-My-time gap between plutonism-metamorphism and mineralization. Econ. Geol. v. 87(7), 1849–1861.
Henry, D.J., Novak, M., Hawthorne, F.C., Ertl, A., Dutrow, B.L., Uher, P., Pezzotta, F., 2011. Nomenclature of the tourmaline-supergroup minerals. Am. Mineral. v. 96(5–6), 895–913.
Jemielita, R., Davis, D., Krogh, T., 1990. U-Pb evidence for Abitibi gold mineralization postdating greenstone magmatism and metamorphism. Nature v. 346(6287), 831.
Jiang, S.Y., Palmer, M.R., Yeats, C.J., 2002. Chemical and boron isotopic compositions of tourmaline from the Archean Big Bell and Mount Gibson gold deposits, Murchison Province, Yilgarn craton. Western Australia. Chemical Geology 188 (3–4), 229–247.
Kerrich, R., King, R., 1993. Hydrothermal zircon and baddeleyite in Val-d'Or Archean mesothermal gold deposits: characteristics, compositions, and fluid-inclusion properties, with implications fortiming of primary gold mineralization. Can. J. Earth Sci.

v. 30(12), 2334–2351.
Kerrich, R., Ludden, J., 2000. The role of fluids during formation and evolution of the southern Superior Province lithosphere: an overview. Can. J. Earth Sci. v. 37(2–3), 135–164.
Krienitz, M.-S., Trumbull, R.B., Hellmann, A., Kolb, J., Meyer, F.M., Wiedenbeck, M., 2008. Hydrothermal gold mineralization at the Hira Buddini Gold Mine, India: contraints on fluid sources and evolution from boron isotopic compositions of tourmaline. Miner. Deposita 43, 421–434.
Lambert-Smith, J.S., Rocholl, A., Treloar, P.J., Lawrence, D.M., 2016. Discriminating fluid source regions in orogenic gold deposits using B-isotopes. Geochim. Cosmochim. Acta 194, 57–76.
Large, R.R., Danyushevsky, L., Hollit, C., Maslennikov, V., Meffre, S., Gilbert, S., Bull, S., Scott, R., Emsbo, P., Thomas, H., 2009. Gold and trace element zonation in pyrite using a laser imaging technique: implications for the timing of gold in orogenic and Carlin-style sediment-hosted deposits. Econ. Geol. v. 104(5), 635–668.
Latulippe, M., 1966. The relationship of mineralization to Precambrian stratigraphy in the Matagami Lake and Val-d'Or districts of Quebec. Geological Association of Canada 3, 21–42.
Lemarchand, J. (2012). Les minéralisations filoniennes aurifères du pluton de Bourlamaque (Val-d'Or, Abitibi): synthèse structurale et apports de la datation 40AR/39AR (Doctoral dissertation, Université du Québec à Montréal).
Marocchi, M., Marschall, H.R., Konzett, J., Tropper, P., Ludwig, T., Mair, V., Bargossi, G.M., 2011. Metasomatic tourmaline in hybrid contact-bands between gneiss and peridotite in the Ulten zone of the Eastern Italian Alps: chemistry and boron isotopic composition. The Canadian Mineralogist v. 49(1), 245–261.
Marschall, H.R., Meyer, C., Wunder, B., Ludwig, T., Heinrich, W., 2009. Experimental boron isotope fractionation between tourmaline and fluid: confirmation from in situ analyses by secondary ion mass spectrometry and from Rayleigh fractionation modelling. Contrib. Miner. Petrol. v. 158(5), 675–681.
Marschall, H.R., Jiang, S.-Y., 2011. Tourmaline isotopes: no element left behind. Elements v. 7(5), 313–319.
Marschall, H.R., Wanless, V.D., Shimizu, N., Pogge von Strandmann, P.A.E., Elliott, T., Monteleone, B.D., 2017. The boron and lithium isotopic composition of mid-ocean ridge basalts and the mantle. Geochim. Cosmochim. Acta 207, 102–138.
McDonough, W.F., Sun, S.-S., 1995. The composition of the Earth: Chemical geology v. 120(3–4), 223–253.
Mériaud, N., Jébrak, M., 2017. From intrusion-related to orogenic mineralization: the Wasamac deposit, Abitibi Greenstone Belt, Canada. Ore Geol. Rev. 84, 289–308.
Meyer, C., Wunder, B., Meixner, A., Romer, R.L., Heinrich, W., 2008. Boron-isotope fractionation between tourmaline and fluid: an experimental re-investigation. Contrib. Miner. Petrol. 156 (2), 259–267.
Molnár, F., Middleton, A., Stein, H., Hugh, O., Lahaye, Y., Huhma, H., Johanson, B., 2018. Repeated syn-and post-orogenic gold mineralization events between 1.92 and 1.76 Ga along the Kiistala Shear Zone in the Central Lapland Greenstone Belt, northern Finland. Ore Geol. Rev. 101, 936–959.
Murowchick, J.B., Barnes, H., 1987. Effects of temperature and degree of supersaturation on pyrite morphology. Am. Mineral. v. 72(11–12), 1241–1250.
Neumayr, P., Hagemann, S.G., 2002. Hydrothermal fluid evolution within the Cadillac tectonic zone, Abitibi greenstone belt, Canada: relationship to auriferous fluids in adjacent second- and third-order shear zones. Econ. Geol. 97, 1203–1225.
Olivo, G.R., Isnard, H., Williams-Jones, A.E., Gariépy, C., 2007. Pb isotope compositions of pyrite from the C quartz-tourmaline vein of the Siscoe gold deposit, Val d'Or, Quebec: Constraints on the origin and age of the gold mineralization. Econ. Geol. 102 (1), 137–146.
Pilote, P., Mueller, W., Scott, C., Lavoie, S., Champagne, C., Moorhead, J., 1998. Volcanologie de la formation de Val-d'Or et du Groupe de Malartic, sous-Province de l'Abitibi: contraintes géochimiques et géochronologiques : Ministère des Ressources naturelles du Québec. DV 98–105.
Rafini, S., 2014. Typologie des minéralisations aurifères associées à la Faille de Cadillac. Rapport du projet CONSOREM 2011-01 et 2012-01, 45 p.
Rezeau, H., Moritz, R., Beaudoin, G., 2017. Formation of Archean batholith-hosted gold veins at the Lac Herbin deposit, Val-d'Or district, Canada: Mineralogical and fluid inclusion constraints. Miner. Deposita 52 (3), 421–442.
Robert, F., Brown, A.C., 1986. Archean gold-bearing quartz veins at the Sigma Mine, Abitibi greenstone belt, Quebec; Part I, Geologic relations and formation of the vein system. Econ. Geol. 81 (3), 578–592.
Robert, F., 1990. Structural setting and control of gold-quartz veins of the Val-d'Or area, southeastern Abitibi subprovince: Gold and base metal mineralization in the Abitibi Sub-Province, Canada, with Emphasis of the Quebec Segment. Geology Department (Key Centre) and University Extension, the University of Western Australia. Publication No. 24, 167–210.
Robert, F., 1994. Vein fields in gold districts: The example of Val-d'Or, southeastern Abitibi subprovince. Geological Survey of Canada, Current Research Paper, Quebec, pp. 295–302.
Robert, F., Boullier, A.M., Firdaous, K., 1995. Gold-quartz veins in metamorphic terranes and their bearing on the role of fluids in faulting. J. Geophy. Res.: Solid Earth 100 (B7), 12861–12879.
Robert, F., Poulsen, K.H., Cassidy, K.F., Hodgson, C.J., 2005. Gold metallogeny of the Superior and Yilgarn cratons. ECONOMIC GEOLOGY 100TH ANNIVERSARY VOLUME, 1001–1033.
Román, N., Reich, M., Leisen, M., Morata, D., Barra, F., Deditius, A.P., 2019. Geochemical and micro-textural fingerprints of boiling in pyrite. Geochim. Cosmochim. Acta 246, 60–85.
Scott, C.R., Mueller, W.U., Pilote, P., 2002. Physical volcanology, stratigraphy, and lithogeochemistry of an Archean volcanic arc: evolution from plume-related volcanism to arc rifting of SE Abitibi Greenstone Belt. Val-d'Or, Canada: Precambrian Research 115 (1), 223–260.
Sibson, R.H., Moore, J.M.M., Rankin, A.H., 1975. Seismic pumping—a hydrothermal fluid transport mechanism. Journal of the Geological Society v. 131(6), 653–659.
Sibson, R.H., Robert, F., Poulsen, K.H., 1988. High-angle reverse faults, fluid-pressure cycling, and mesothermal gold-quartz deposits. Geology v. 16(6), 551–555.
Swihart, G.H., Moore, P.B., 1989. A reconnaissance of the boron isotopic composition of tourmaline. Geochim. Cosmochim. Acta v. 53(4), 911–916.
Trumbull, R.B., Slack, J.F., 2018. Boron isotopes in the continental crust: granites, pegmatites, felsic volcanic rocks and related ore deposits. In: In: In: Marschall, H.R., Foster, G.L. (Eds) Boron,, . (Ed.), Isotopes - The Fifth Element. Advances in Geochemistry v. 7. Springer, Heidelberg, pp. 249–272.
Van Hinsberg, V.J., Schumacher, J.C., 2009. The geothermobarometric potential of tourmaline, based on experimental and natural data. Am. Mineral. v. 94(5–6), 761–770.
Wang, L., Shi, X., Jiang, G., 2012. Pyrite morphology and redox fluctuations recorded in the Ediacaran Doushantuo Formation. Palaeogeogr. Palaeoclimatol. Palaeoecol. 333, 218–227.
Wong, L., Davis, D., Krogh, T., Robert, F., 1991. UPb zircon and rutile chronology of Archean greenstone formation and gold mineralization in the Val-d'Or region, Quebec. Earth Planet. Sci. Lett. v. 104(2–4), 325–336.
Zhang, J., Deng, J., Chen, H.-Y., Yang, L.-Q., Cooke, D., Danyushevsky, L., Gong, Q.-J., 2014a. LA-ICP-MS trace element analysis of pyrite from the Chang'an gold deposit, Sanjiang region, China: Implication for ore-forming process. Gondwana Res. 26 (2), 557–575.
Zhang, J., Linnen, R., Lin, S., Davis, D., Martin, R., 2014b. Paleoproterozoic hydrothermal reactivation in a Neoarchean orogenic lode-gold deposit of the southern Abitibi subprovince: U-Pb monazite geochronological evidence from the Young-Davidson mine, Ontario. Precambr. Res. 249, 263–272.